Received: 28 August 2022 | Revised: 9 November 2022 | Accepted: 10 November 2022

DOI: 10.1002/eom2.12312

RESEARCH ARTICLE

EcoMat FUNCTIONAL MATERIALS FOR GREEN ENERGY AND ENVIRONMENT WILEY

Rational engineering of metal–organic coordination networks into facet-controlled phosphides for overall water splitting

Gamze Yilmaz[1] | **Tong Yang**[2] | **Kane Jian Hong Lim**[1] | **See Wee Chee**[3,4,5,6] | **Lei Shen**[7] | **Utkur Mirsaidov**[3,4,5,6] | **Michel Bosman**[6] | **Ghim Wei Ho**[1,6]

[1]Department of Electrical and Computer Engineering, National University of Singapore, Singapore, Singapore

[2]Department of Applied Physics, The Hong Kong Polytechnic University, Hong Kong SAR, China

[3]Department of Physics, National University of Singapore, Singapore, Singapore

[4]Centre for Bioimaging Sciences and Department of Biological Sciences, National University of Singapore, Singapore, Singapore

[5]Centre for Advanced 2D Materials and Graphene Research Centre, National University of Singapore, Singapore, Singapore

[6]Department of Materials Science and Engineering, National University of Singapore, Singapore, Singapore

[7]Department of Mechanical Engineering, National University of Singapore, Singapore, Singapore

Correspondence
Ghim Wei Ho, Department of Electrical and Computer Engineering, National University of Singapore, 4 Engineering Drive 3, Singapore 117583, Singapore.
Email: elehgw@nus.edu.sg

Funding information
Ministry of Education (MOE) Singapore, under AcRF Tier 2, Grant/Award Number: MOE2019-T2-1-179; NUS R&G Postdoc Fellowship Programme, Grant/Award Number: A-0000065-44-00; A*STAR under its 2019 AME IRG & YIRG Grant Calls, Grant/Award Number: A2083c0059

Abstract

Although transition metal phosphide electrocatalysts display unique electronic structure that serves as functional centers for hydrogen evolution reaction, the synthesis of this class of materials for oxygen evolution remains a challenge due to the complex multielectron transfer pathways and sluggish reaction kinetics. This study details an in-situ modification and transformation of cyanide-bridged nickel-iron (CN-NiFe) organometallic hybrid into the preferential Fe_2P phase with prevailing exposed $\{1\bar{2}0\}$ faceted active centers by leveraging on the facile coordinate cleavage dynamics and compound reactivity of labile metal organic coordination frameworks. The resultant transition metal phosphide attains high electrochemical surface area, low Tafel slope, and low overpotential for the oxygen evolution reaction, while also demonstrating bifunctional electrocatalytic performance for overall water splitting. Comprehensive experimental studies and density functional theory calculations reveal that the exceptional catalytic activity originates from the transformation of framework metallic sites into preferential active sites allows an optimal adsorption of oxygen evolution reaction intermediates.

KEYWORDS

electrocatalyst, metal-organic framework, Prussian blue analogue, phosphide, water splitting

---

Gamze Yilmaz, Tong Yang, and Kane Jian Hong Lim contributed equally to this work.

1 | INTRODUCTION

Water splitting offers a promising and sustainable solution to alleviate future global energy demands for affordable and reliable energy generation and storage, such as through hydrogen production, rechargeable metal-air batteries, and fuel cells.[1–4] Thermodynamically, under standard conditions, water splitting is an endergonic reaction requiring an activation energy of 286 kJ mol^{-1}, which is achievable via electrolysis. Unfortunately, to attain appreciable current densities after reaction activation, high overpotentials are generally needed due to the sluggish half-cell reaction kinetics, namely, the hydrogen evolution reaction (HER) and the oxygen evolution reaction (OER).[5–8] Although noble metals exhibit unrivaled catalytic performances as benchmark water-splitting electrocatalysts (IrO_2 for OER and Pt for HER), their low abundance and high cost greatly hinder large-scale applications.[9,10] Besides, it can also be challenging and costly to pair two different monofunctional catalysts as the anodic and cathodic half-cells to form an integrated water-splitting cell. Hence, though challenging, it is highly important to rationally design non-precious and highly active bifunctional electrocatalysts.

Considerable progress has been achieved in the last decade to explore promising alternative nonprecious HER and OER electrocatalysts including transition metal oxides/hydroxides,[11,12] sulfides,[11,13–15] phosphides,[14,16,17] selenides,[13,18] nitrides,[19,20] carbides,[21,22] and borides.[22] Among them, transition metal phosphides (TMPs) have been widely explored as HER catalysts owing to the resemblance of their electronic structure to hydrogenases, which are highly active H_2 generating enzymes, and their promising catalytic performances toward the hydrodesulfurization reaction.[23,24] Using detailed molecular calculations, the superb catalytic performance of TMPs toward HER has been ascribed to the ensemble effect that allows a moderate hydrogen binding environment on active sites due to the direct involvement of phosphorous in the reaction. In addition, the decreased poisoning effect of the metallic species creates favorable proton-acceptor (phosphorus) and hydride-acceptor (metal) sites.[23,24] However, compared to HER, OER has been the bottleneck because of the multielectron transfer pathways and complex reaction steps involving successive formation of three different adsorption intermediates (OOH*, O*, and OH*).

Nevertheless, prominent improvement in OER activity can be realized via atomic engineering since the crystallographic orientations, coordination number of atoms and number of dangling bonds greatly affect the catalytic reactivity of nanocrystals.[25,26] Essentially, highly active sites generally transpire in a local environment and orientation in the form of high surface energy facets. Nanocrystals meticulously elaborated by such active facets with favorable electronic structure can ensure thermodynamically and kinetically favorable surface adsorption and reaction, which warrants an utmost exploitation of the catalytic activity. However, typical nanocrystals are generally enclosed by diverse crystal planes, exposing different facets with dissimilar activities, and thereby reducing the overall electrocatalytic activity. Moreover, although creating highly reactive facets is a particularly enticing route for designing advanced electrocatalysts, they are difficult to be preserved as a result of these same high surface energies. Thus, the development of reliable and ingenious surface structural approaches to create a selective favorable surface atomic arrangement is an exciting breakthrough and fundamentally important to exploring new active and stable facets for high performing electrocatalysis. Specifically, rational synthesis of transition metal phosphides to explore and reveal the aforementioned surface atomic features that are beneficial for OER have not been well-explored thus far, despite the great progress achieved in investigating their HER activities.

Here, we devise a controllable reductive alkaline etching strategy to modify the framework chemistry and reactivity in the metal–organic coordination network of Prussian blue analogues (PBAs) by exploiting the lability of metal centers and metal–ligand bonds. The as-etched classical crystals of PBAs are conceived to comprise the original synergistic organometallic hybrid, that is, inorganic superstructures with atomically coordinated organic cyanide (CN) bridges in congruence with altered coordinate cleavage dynamics and compound reactivity. Based on the refined framework chemistry, bimetallic transition metal content and weak intramolecular bonds, we formulated a non-destructive phosphorization and preferential manifestation of a transition metal phosphide phase with predominantly active facets. Significantly, unlike the pristine PBAs that susceptibly reconstitute a variant of planes after phosphorization because of the comparable reactivity of its transition metal sites, the refined as-etched PBAs readily transform into a favorable phosphide phase with prevailing reactive centers. Explicitly, for the first time, we disclose a facile and efficient strategy to prepare the Fe_2P phase with primarily exposed $\{1\bar{2}0\}$ facets that we prove to possess high OER activity, using proof-of-concept electrochemical tests and theoretical studies. Notably, using this methodology, it is possible to judiciously engineer similar iron-containing PBAs into iron phosphides with the same exposed active facets. Thus, the in-situ tailoring of the atomic bonding and crystal structure to synthetically modify phosphides and consequently unravel prominent OER active sites; can be recognized as a pioneering strategy for the design of new advanced OER electrocatalysts.

2 | RESULTS AND DISCUSSION

A template-engaged strategy is employed to prepare nickel-iron phosphide nanocrystals with primarily exposed high-index $\{1\bar{2}0\}$ facets of iron phosphide. The preparation of nickel-iron phosphide includes three successive steps: (i) preparation of self-sacrificial templates, (ii) etching and (iii) phosphorization (Figure S1). Essentially, classical crystals of nickel-iron (Ni—Fe) PBAs are selected as the self-sacrificial templates due to their location-dependent etching stability, robustness, low-degree of defects, high-degree of lability, favorable dynamic framework and bimetallic transition metal content.[27,28] In this study, the self-sacrificial templates manifest sufficiently strong chemical stability to allow a kinetically controlled chemical etching process while being prone to changes in the microstructural features. In addition, it remains structurally intact during the phosphorization step at high temperatures. The PBAs are first synthesized via a facile coprecipitation process in an aqueous solution containing $K_3Fe(CN)_6$ and $Ni(NO_3)_2{\cdot}6H_2O$.[29] The morphology of the as-synthesized PBAs are investigated by field-emission scanning electron microscopy (FESEM) and transmission electron microscopy (TEM) as shown in Figure 1A and D, respectively. The PBAs exhibit uniform cubic structure and a narrow size distribution with an average particle size of 180 nm (Figures S2–S3). The flat external faces and edges of the nanocubes, as revealed by TEM, suggests the formation of NiFe-PBAs nanocubes through the classical ionic/molecular crystallization pathway. This signifies the absence of mesocrystalline features dominated by clustered subunits that are formed by oriented crystallographic fusion of primary nanocrystal building units. Although mesocrystals and classical crystals of PBAs show identical single-crystal features, mesocrystals possess much weaker stability due to a void-rich, mostly defective structure with discontinuous and broken grain boundaries, which makes a chemical etching process difficult to control. Here, the compact and less-defective

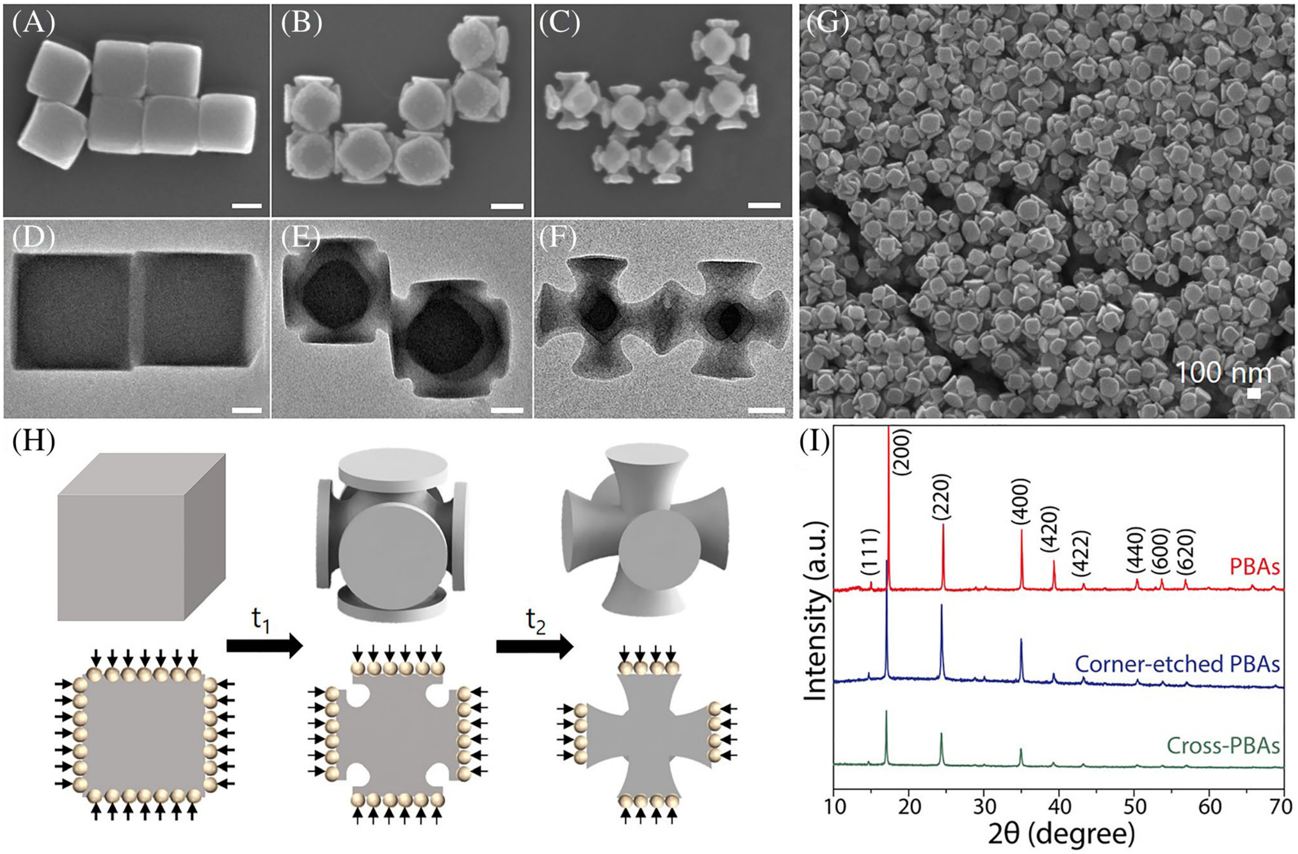

FIGURE 1 Morphological and structural characterizations of the Prussian blue analogues (PBAs) and etched-PBAs. Scanning electron microscopy (SEM) images of the (A) PBAs, (B) corner-etched PBAs, and (C) cross-PBAs. The scale bar shows 100 nm. Transmission electron microscopy (TEM) images of the (D) PBAs, (E) corner-etched PBAs, and (F) cross-PBAs. The scale bar shows 50 nm. (G) SEM image shows the uniform and preferential etching of PBAs. (H) Schematics illustrating the structural evolution of the cross-shaped PBAs from PBA nanocubes. t_1 and t_2 represent 3 and 6 h, respectively, the time required for the formation of the structures. (I) Corresponding X-ray diffraction (XRD) profiles of the structures.

NiFe-PBAs crystals permit the gradual development of corner-etched PBAs (Figure 1B, E) and finally cross-PBAs (Figure 1C, F) through the chemical etching process (Figures S1 and S2). The etching on PBAs is observed to be appreciably uniform and occurs preferentially on the corners and edges that possess high-surface energy and more reactivity (Figure 1G). Figure 1H illustrates the structural evolution of the cross-shaped PBAs from PBAs nanocubes at 3 and 6 h, respectively. The average particle sizes of the corner-etched PBAs (166 nm) and cross-PBAs (163 nm) do not change significantly (Figures S3–S7), indicating low etching activity on the {100} planes of the PBAs. The selective etching of the corners and edges of the PBAs is attained by a kinetically controllable alkaline etching approach (Figure S8). By adding potassium hydroxide (KOH) and trisodium citrate (Na_3Cit) to a suspension of PBAs, corner-etched PBAs and cross-PBAs are obtained after 3 and 6 h, respectively, at room temperature. The structural evolution of PBAs is kinetically driven by cooperative engraving of the etching components. Basically, treatment of PBAs with Na_3Cit in the absence of KOH does not alter the size and morphology of the PBAs, while etching takes place rather slowly when the PBAs are treated using KOH without Na_3Cit (Figure S8). In particular, KOH alone slightly carves the edges and corners of the cubes revealing the regions less stable in alkaline solution, as also demonstrated in previous studies.[30,31] At the same regions, the etching rate of KOH can be effectively triggered by adding Na_3Cit, a well-known complexing agent which can directly coordinate to various transition metal sites.[32–34] In this process, we postulate that while the alkaline etching proceeds through to cleave the labile Ni^{II}—$[Fe^{II/III}(CN)_6]$ complex in the framework, citrate molecules quickly interact with the nickel in the disassembled framework. This weakens the coordination strength of the cyanide ligand in the as-formed hemilabile PBAs due to the formation of a stronger metal-carboxylate π-bonding, and thus allows a facile subsequent alkaline etching process.[35–37] Moreover, the relative amounts of the KOH and Na_3Cit is a crucial factor determining the kinetics of the etching. If either etchant component participates at low concentration, etching takes place rather slowly, producing cubes with poorly defined cavities (Figure S9). In contrast, when the concentration of either etchant is high, broken particles are obtained (Figure S9). This phenomenon shows that controllable etching depends on a balanced citrate coordination-alkaline carving process. Similarly, PBAs can be etched using an equivalent concentration of NaOH as an alternative to KOH, affirming the generalization of the citrate coordination-alkaline carving process (Figure S10).

The effect of etching treatment on the microstructural bonding properties of the PBAs is examined by Fourier transform infrared spectroscopy (FTIR) and shown in Figure S11A. The FTIR spectrum of PBAs exhibits two prominent peaks at 2165 and 2099 cm^{-1} originating from the stretching vibrations of Fe^{III}—CN—Ni^{II} and Fe^{II}—CN—Ni^{II}, respectively.[38] As compared with the pristine PBAs, the corner etched-PBAs shows only one sharp stretching band at a wavenumber of 2092 cm^{-1}, indicating the sole presence of Fe^{II}—CN—Ni^{II} in the etched structures. Notably, there occurs a slight shift in the original Fe^{II}—CN—Ni^{II} peak position, which is related to the additional potassium ions introduced to the interstitial sites (Figure S11B) to maintain the electroneutrality of the structure during the reductive etching process.[39] Here, the FTIR study clearly reveals that etching treatment reduces the oxidation state of Fe in PBAs from Fe^{III} to Fe^{II}. Moreover, X-ray photoelectron spectroscopy (XPS) investigation for the Fe 2p region of PBAs and corner-etched PBAs also confirms the reduction of the iron oxidation state after the etching process (Figure S12). The crystal structure and phase purity of the PBAs and the etched products are examined by X-ray diffraction (XRD) as shown in Figure 1I. Both PBAs and etched PBAs (corner-etched PBAs and cross-PBAs) exhibit sharp and strong peaks with similar XRD patterns with slightly different lattice parameters (10.29 and 10.37 Å, respectively), showing that the pure face-centered cubic phase of nickel-iron PBAs (JCPDS card no. 86-0501) is mostly retained during the etching treatment. The change in lattice parameter can be attributed to the increase in the radius of CN-coordinated iron during their reduction from iron (III) to the iron (II), and to an increase in the number of potassium ions.[40,41] Moreover, the absence of a hydroxide phase in the XRD patterns of the etched products eliminates the possibility of an ion exchange reaction between the hydroxide ions with the PBAs.[42]

The PBAs-P, corner-etched PBAs-P and cross-PBAs-P are converted from the as-obtained nickel iron PBA coordination networks via the decomposition of a phosphorous source, NaH_2PO_2, at 300°C in argon atmosphere, and its reaction with the PBAs, corner-etched PBAs and cross-PBAs, respectively. SEM images in Figures 2A and S13 show the non-destructiveness of the phosphorization treatment under the selected reaction conditions by virtue of the kinetically labile metal–ligand linking-breakage of the coordination compound. Further SEM (Figure 2A) and TEM (Figure 2B) investigations of the corner-etched PBAs-P also reveal that the morphology of the corner-etched PBA precursors is well-retained during the phosphorization treatment. The presence of Fe, Ni, and P elements and their homogeneous distribution in the products are confirmed by the scanning transmission electron microscopy-electron energy loss spectroscopy (STEM-EELS) elemental mapping as shown in

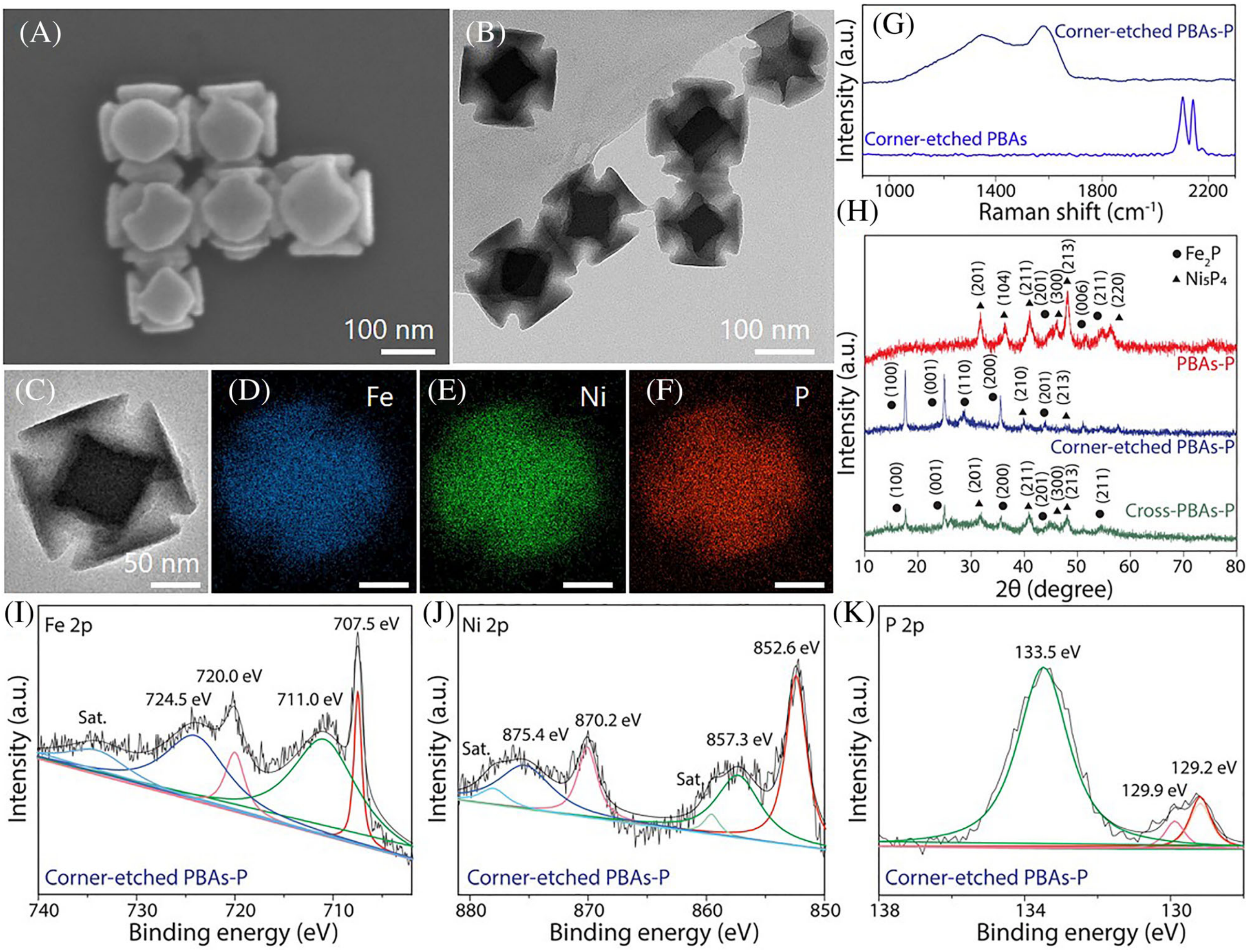

FIGURE 2 Morphological and structural characterizations of the corner-etched PBAs-P. (A) Scanning electron microscopy (SEM) and (B) Transmission electron microscopy (TEM) image of corner-etched PBAs-P. (C) TEM image of a corner-etched PBA-P nanoparticle, and the corresponding STEM-EELS elemental mapping of (D) iron, (E) nickel and (F) phosphorus elements. (G) Raman spectrum and (H) X-ray diffraction (XRD) patterns of the corner-etched PBAs-P. High-resolution (I) Fe 2p, (J) Ni 2p and (K) P 2p XPS spectra of the corner-etched PBAs-P.

Figure 2C–F. In addition, energy dispersive X-ray spectroscopy (EDX) and XPS further corroborate the presence of Ni, Fe, and P elements as well as carbon and nitrogen in the corner-etched PBAs-P (Figure S14).

To investigate the extent of topological transformation of the PBA coordination compound into a phosphide phase and examine the nature of the carbon in the corner-etched PBAs-P, Raman spectroscopy, XRD and high-resolution XPS are carried out. The Raman spectrum of the corner-etched PBAs in Figure 2G displays two distinct peaks at 2100 and 2143 cm^{-1}, which are assigned to the stretching vibration of $\mathrm{Fe}^{\mathrm{II}}$-coordinated carbon nitrogen.[43] On the other hand, in the spectrum of corner-etched PBAs-P, no obvious cyanide bands are detected, supporting the complete decomposition of the carbon-nitrogen coordination. The bands displayed at 1350 and 1583 cm^{-1} indicate the typical D- and G-bands, respectively,[44,45] which, in conjunction with XPS and EDX, suggests the emergence of graphitic properties of N-doped-carbon with the phosphorization treatment. The crystal structures of the phosphorization products are analyzed using XRD (Figure 2H). The XRD profiles of the products clearly reveal the disappearance of the NiFe-PBA phase (Figure 1I) and formation of new crystal phases, further confirming the synergistic efficacy of the phosphorization treatment and favorable dynamics of the Ni-Fe coordination network. The XRD pattern of PBAs-P can be indexed to be a mixture of $\mathrm{Ni_5P_4}$ (JCPDS no. 18-0883) and $\mathrm{Fe_2P}$ (JCPDS no. 88-1803) phases, with $\mathrm{Ni_5P_4}$ as the major component.[46,47] Although the XRD spectra of corner-etched PBAs-P and cross-PBAs-P also display the diffraction features of the mixed $\mathrm{Ni_5P_4}$ and $\mathrm{Fe_2P}$ phases, the $\mathrm{Fe_2P}$ phase emerges as the major component. Importantly, different from the XRD pattern of

PBAs-P, two additional characteristic peaks occur at 17.6° and 25.4°, corresponding to the (100) and (001) crystal planes of hexagonal Fe_2P. This activation of the iron phosphide phase in the etched-structures can be elucidated by the modification of the framework chemistry.

The coordination stability of the metallic components and cyanide ligand modified in the course of the initial PBA etching process eventually affects the bond-breaking dynamics and reactivity of the components during the final phosphorization treatment. Particularly, metal–ligand bond strength in cyanide coordinated frameworks is directly affected by the oxidation states of the metals.[36,37,48] As Fe^{III}—CN exhibits larger metal-carbon and carbon-nitrogen force constants (strengths) than Fe^{II}—CN, since it experiences a stronger metal-carbon σ-bond and CN bond.[36,37,48] This relative weakness of the coordinate bond in the etched samples that contain Fe^{II}—CN, allows the readily cleavage of Fe—C and C—N linker bonds and a kinetically facile reaction of iron with phosphorus. Therefore, the Fe_2P crystal phase actively develops in corner-etched PBAs-P and cross-PBAs-P, whereas the Ni_5P_4 crystal structure occurs as the major component in PBAs-P. Similarly, by using the devised method, we also modified the crystalline properties of cobalt-iron PBAs to disclose the Fe_2P crystal planes (Figures S15–S16). The oxidation state of the iron in the cobalt-iron PBAs was completely reduced to 2+ from 3+ by the same etching treatment, and the as-etched material was subsequently converted to a mixture of Fe_2P and CoP crystal phases, with Fe_2P as the major component. This indicates the adaptability of the approach, which is highly significant considering the large diversity of bimetallic iron-based PBAs.

X-ray photoelectron spectroscopy measurements are further carried out to probe the surface composition and the oxidation state of the phosphide products as shown in Figures 2I–K and S17. The high-resolution Fe 2p spectrum in Figure 2I shows two peaks, at 707.5 and 711.0 eV located in the Fe $2p_{3/2}$ region, whereas the Fe $2p_{1/2}$ region consists of two peaks at 720.0 and 724.5 eV, along with a satellite peak. The peaks at 707.5 and 720.0 eV are assigned to binding energies of Fe_2P, and the other peaks can be attributed to oxide binding energies due to superficial surface oxidation of phosphides.[49,50] In the Ni 2p spectrum of corner-etched PBAs-P (Figure 2J), the two peaks at 852.6 and 870.2 eV correspond to the Ni $2p_{3/2}$ and Ni $2p_{1/2}$ energy levels of Ni_5P_4, respectively. Meanwhile, the peaks located at 857.3 and 875.4 eV, which are accompanied by a satellite peaks, are consistent with oxidized Ni species.[47,51] The high-resolution P 2p spectrum in Figure 2K is deconvoluted into two peaks, located at 129.2 and 129.9 eV, corresponding to the P $2p_{3/2}$ and P $2p_{1/2}$ binding energies of reduced phosphorous in metal phosphides. Moreover, the peak occurring at 133.5 eV reflects the P—O bonding (P^{5+}) on the surface, which explains the conspicuous oxygen peak observed in the XPS survey scan.[47,50,52] Noticeably, the binding energies of nickel and iron are positively shifted compared to those of metallic nickel (852.5 eV) and iron (706.7 eV), while the binding energy of the measured phosphorus peak is lower than that of elemental phosphorus (130.1 eV). This indicates the partial positive charge of nickel and iron, and partial negative charge of phosphorus in the phosphorization products, confirming the formation of a bimetallic phosphide phase.

The electrocatalytic OER activities of the PBAs compounds and their phosphorization products are investigated in 1 M KOH aqueous electrolyte. Figure 3A shows the polarization curves of the PBAs, corner-etched PBAs, cross-PBAs, PBAs-P, corner-etched PBAs-P and cross-PBAs-P obtained by linear sweep voltammetry (LSV) at a scan rate of 5 mV s^{-1} in the potential window of 1.2–1.85 V (vs. RHE). Compared to PBAs and etched PBAs (corner-etched PBAs and cross-PBAs), which are presented by dashed-lines, their phosphide derivatives (solid lines) exhibit greatly improved OER activities, demonstrating that the phosphorization treatment effectively modulates the electrocatalytic inertness of PBA compounds and elaborates the final crystal structure with highly exposed active sites. Among the phosphide derivatives, the corner-etched PBAs-P shows the best performance, with a small onset oxidation potential of 1.46 V and an overpotential of 260 mV at the anodic current density of 10 mA cm^{-2}. Notably, it only requires overpotentials of 310 and 350 mV to reach the current densities of 50 and 100 mA cm^{-2}, respectively. Comparatively, to attain 10 mA cm^{-2}, cross-PBAs-P, PBAs-P, corner-etched PBAs, cross-PBAs and PBAs require relatively higher overpotentials of 300, 314, 384, 390, and 397 mV, respectively (Table S1). The electrochemical OER kinetics of the catalysts is assessed by the Tafel slopes obtained from the Tafel plots (Figure 3B). The Tafel slope of corner-etched PBAs-P is measured to be 45 mV dec^{-1}, which is superior to that of cross-PBAs-P (51 mV dec^{-1}) and PBAs-P (57 mV dec^{-1}), and significantly lower than that of PBAs and etched PBAs, revealing the favorable OER kinetics of corner-etched PBAs-P. Figure 3C explicitly presents the Tafel slope-overpotential (at 10 mA cm^{-2}) relation of PBAs and their phosphide counterparts. The phosphides are located at a low Tafel slope-low overpotential region, which confirms the prominent activation of the PBAs with phosphorization treatment. Particularly, better electrocatalytic OER performances of the corner-etched PBAs-P and cross-PBAs-P than that of PBAs-P reveals the further emergence of the catalytically active sites and enhancement of the intrinsic OER activity via

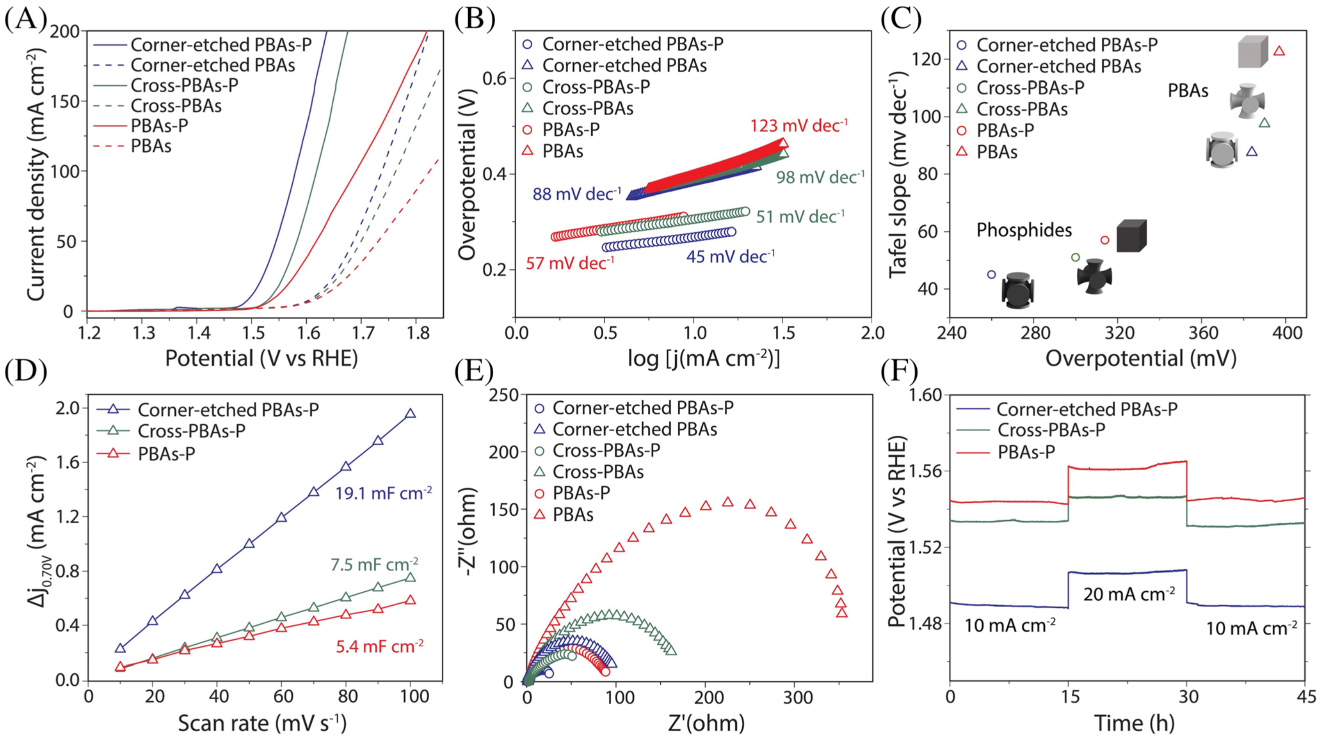

FIGURE 3 Electrocatalytic oxygen evolution reaction (OER) performance of pristine Prussian blue analogue (PBA) compounds and their phosphorization products. (A) OER polarization curves recorded at a scan rate of 5 mV s^{-1} in 1 M KOH. (B) Corresponding Tafel plots of the electrocatalysts in (A). (C) Tafel slopes against overpotentials at a current density of 10 mA cm^{-2}. (D) Estimation of double layer capacitances of PBAs-P, corner-etched PBAs-P and cross-PBAs-P using the capacitive current densities at 0.7 V (vs. RHE) as a function of scan rates. (E) Nyquist plots. (F) Time dependence of the voltage under static current densities of 10 and 20 mA cm^{-2} over 45 h of continuous operation.

the etching treatment. Specifically, the corner-etched PBAs-P, which showed the lowest overpotentials, had exhibited a mass activity of 27.3 A g^{-1} and a high turnover frequency (TOF) of 3.18 s^{-1} at 350 mV overpotential (Figure S18). The electrochemical active surface area (ECSA) further serves as another relevant measure for an assessment of the catalytic activity. The ECSA values are obtained from the cyclic voltammograms of the PBAs-P, corner-etched PBAs-P and cross-PBAs-P collected at various scan rates (10–100 mV s^{-1}) (Figures S19 and 3D). Corner-etched PBAs-P and cross-PBAs-P possess ECSA values of 19.1 and 7.5 mF cm^{-2}, which are 3.5 and 1.4 times higher than that of the PBAs-P, respectively. This clearly supports the enriched catalytically active sites in the etched-phosphides.

Nyquist plots obtained from the electrochemical impedance spectroscopy (EIS) tests are shown in Figure 3E. The phosphide derivatives exhibit smaller semicircles compared to the pristine counterparts, thus they possess smaller charge transfer resistances. This can be ascribed to the realization of more favorable charge transport kinetics with the in-situ generation of N-doped-graphitic carbon during the high temperature phosphorization treatment as shown in Figure 2G. Moreover, the long-term electrochemical stability of PBAs-P, corner-etched PBAs-P and cross-PBAs-P electrocatalysts is examined by chronopotentiometric measurements by applying consecutive constant current densities of 10, 20, and 10 mA cm^{-2}, and investigating the changes between the initial and resulting potentials during 45 h of continuous OER operation. As presented in Figure 3F, in general, PBAs-P, corner-etched PBAs-P and cross-PBAs-P show negligible voltage degradation after 45 h. Notably, after the second 15 h of operation at the higher current density of 20 mA cm^{-2}, the electrocatalysts could deliver the same potential at 10 mA cm^{-2} as the initial potential delivered after 1 h, implying their outstanding electrochemical stability.

To gain insight into the enhanced electrochemical activity of the corner-etched PBAs-P, the crystalline nanostructures are investigated by high-resolution TEM (HR-TEM) measurements. Typical TEM images of the corner-etched PBAs-P are given in Figures 4A and S20, showing the homogeneity of the nanoparticles with sharp edges, corners and well-defined faces. HRTEM images taken from the regions A, B, C, and D are presented in

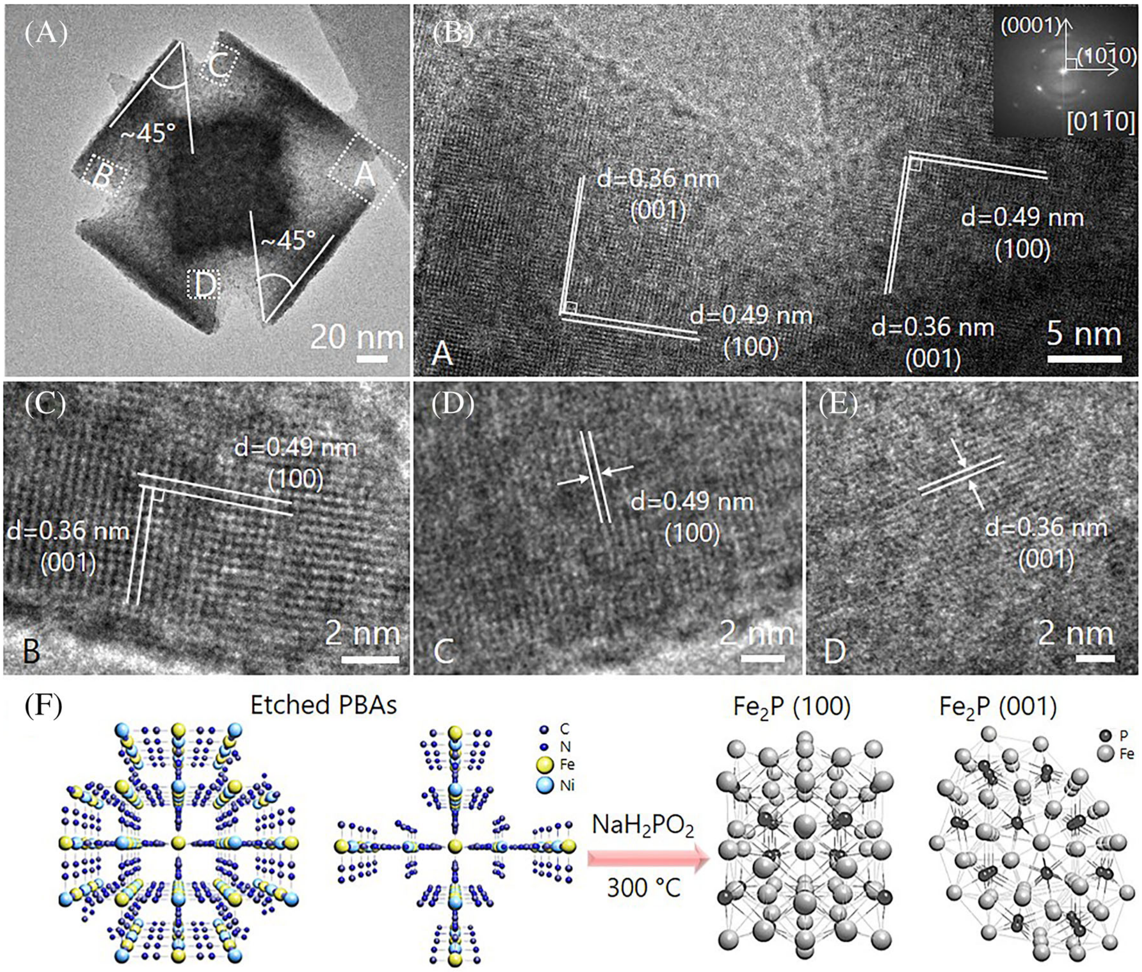

FIGURE 4 High-resolution transmission electron microscopy (HR-TEM) characterizations of the corner-etched PBAs-P (A) TEM image of a corner-etched PBA-P nanoparticle and high-resolution TEM images from (B) region A, (C) region B, (D) region C, and (E) region D. (F) Atomic representation of the etched PBA structures before and after the phosphorization process.

Figure 4B, C, D, and E, respectively. Strikingly, the corner-etched PBAs-P are enclosed with two neighboring (100) and (001) facets of Fe_2P with interlayer spacings of 0.49 and 0.36 nm, respectively, separated by an interfacial angle of approximately 90° (Figure S21), consistent with the observations in the XRD studies in Figure 2H. This suggests that the primarily exposed facet of the corner-etched PBAs-P is $\{1\bar{2}0\}$ (Figure S22), which is further confirmed by the fast Fourier transform image (Figure 4B inset). In comparison, for pristine PBAs that did not undergo chemical etching, HRTEM images of their phosphorization product (PBAs-P) show an assortment of planes in random orientations (Figure S23). Moreover, it was noted that even after long-term OER testing, the neighboring (100) and (001) planes were still clearly visible in the HRTEM images of the corner-etched PBAs-P, suggesting good stability of the exposed facet, and further substantiates the electrochemical stability of corner-etched PBAs-P (Figure S24). Figure 4F presents the atomic arrangement of the etched PBA structures before and after the phosphorization process to illustrate etched PBAs with the two enclosed adjacent (100) and (001) facets of Fe_2P.

To understand the compositional dependent OER activity of nickel-iron phosphides, where corner-etched PBAs-P (major component: Fe_2P) is much superior to PBAs-P (major component: Ni_5P_4), density functional theory (DFT) calculations were performed. Previous experimental and theoretical reports have confirmed that the adsorption of oxygenated intermediates (especially *OH) is the rate-determining step in OER for metal phosphides.[53–55] The optimization of *OH adsorption on metal phosphides is thus critical for the rational design of high-performance OER catalysts.[55] Therefore, we calculated the *OH adsorption energies on the surfaces of Fe_2P and Ni_5P_4 (Figure 5A, B). The Fe_2P $\{1\bar{2}0\}$ facet is chosen since it is primarily exposed in the corner-etched PBAs-P (Figures 4 and 5A). It is found that all of the surface Fe

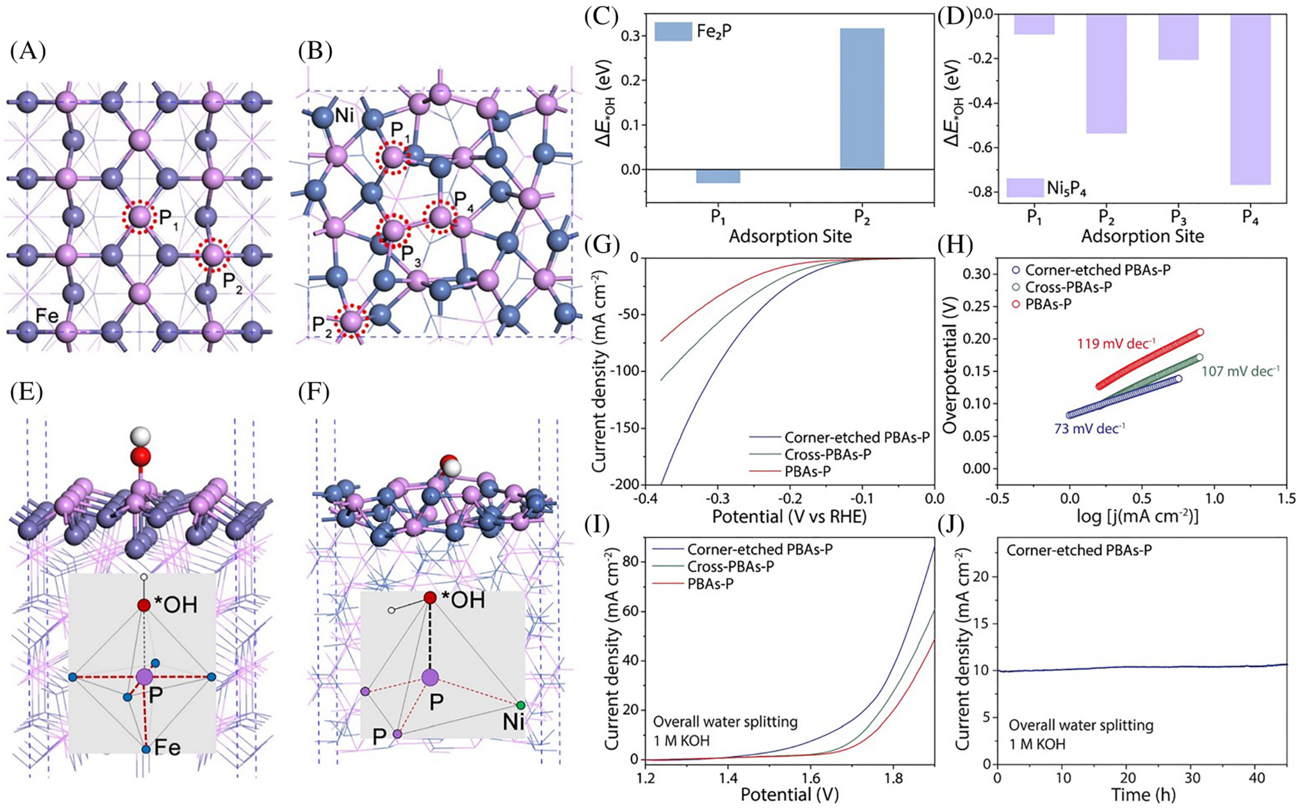

FIGURE 5 Density functional theory (DFT) simulations, and the electrocatalytic hydrogen evolution reaction (HER) and overall water splitting performances. The top view of the $(1\bar{2}0)$ facet of (A) Fe_2P and (B) Ni_5P_4. The potential adsorption sites are marked by red dashed circles. The atoms near the surface are visualized in the ball-stick mode and other atoms in line mode. (C–D) The adsorption energy of *OH intermediate on (C) the Fe_2P facet and (D) the Ni_5P_4 facet. (E–F) A tilted side view of the most stable *OH adsorption on (E) Fe_2P and (F) Ni_5P_4. The inset in (E) and (F) are the local configuration of *OH absorption. (G) HER polarization curves recorded at a scan rate of 5 mV s^{-1} in 1 M KOH. (H) Corresponding Tafel plots. (I) Polarization curves for overall water splitting obtained using a two-electrode system at a scan rate of 5 mV s^{-1} in 1 M KOH. (J) Chronoamperometric test of the corner-etched PBAs-P catalyst for 45 h at an applied potential of 1.64 V.

sites are unable to stabilize the *OH adsorbate. Upon structural relaxations, the *OH adsorbate will migrate to the surface phosphorus sites, implying that the latter are the active adsorption sites. Figure 5C shows the calculated *OH adsorption energy on distinct phosphorous sites (marked in Figure 5A). Site P_1 is the favorable adsorption site with an adsorption energy of −0.030 eV, whereas at the P_2 site it is 0.316 eV. This value is comparable to −0.058 eV that was previously calculated for strained FeP_2.[55] Next, the adsorption energy of *OH on the same facet of Ni_5P_4 was calculated for comparison (Figure 5B). As shown in Figure 5D, the most stable *OH adsorption takes place on the site P_4 with an adsorption energy of −0.765 eV, such a negative adsorption energy however suggests that Ni_5P_4 adsorbs *OH too strongly for OER. In contrast, the moderate *OH adsorption energy of Fe_2P is more favorable and translates to a superior electrocatalytic performance. The relatively weaker *OH adsorption on Fe_2P compared with Ni_5P_4 can be understood by their different adsorption configurations (Figure 5E, F). In an octahedron-like configuration for *OH adsorption on Fe_2P (Figure 5E), the orbitals of the surrounding five atoms (Figure 5E, small blue atoms) are toward the central P atom (Figure 5E, purple atom). Such a stable configuration in Fe_2P results in its moderate *OH adsorption. In contrast, for the tetrahedron-like configuration of Ni_5P_4, the orbital directions are not toward the central atom (Figure 5F), leading to a strong *OH adsorption on Ni_5P_4.

Phosphide-based transition metal electrocatalysts have been well-investigated for HER as the negatively charged phosphorous can offer extra active sites to trap the positively charged protons and modulate the transition metal-phosphide bonds for more favorable hydrogen adsorption on the transition metal site.[23,56] However, phosphide-based transition metals are less-often reported as superior electrocatalysts for OER in alkaline media due to their sluggish reaction kinetics. Considering the superior OER performance of the corner-etched PBAs in alkaline media and promising HER activity of metal phosphides, we now assess the HER electrocatalytic activity of corner-etched PBAs for developing a bifunctional OER and HER catalyst for overall water splitting. The HER activity of the corner-etched PBAs-P is evaluated by LSV in 1 M KOH aqueous electrolyte at a scan rate of 5 mV s^{-1} (Figure 5G). It delivers a cathodic current density of 10 mA cm^{-2} at an overpotential of 145 mV, which was lower compared to that of cross-PBAs-P and PBAs-P which required 182 and 221 mV, respectively. Additionally, corner-etched PBAs also exhibits the lowest Tafel slope of 73 mV dec^{-1}, while Tafel slopes of 107 and 119 mV dec^{-1} were recorded for cross-PBAs-P and PBAs-P, respectively (Figure 5H). In addition, the overpotential and Tafel slope of the corner-etched PBAs-P are better or comparable to that of other similar phosphide-based electrocatalysts assessed in alkaline media, such as iron phosphide nanoparticles,[57] Ni_5P_4 films,[58] porous iron-doped cobalt phosphide polyhedrons,[59] ultrasmall diiron phosphide nanodots anchored on graphene sheets,[60] and iron-tuned super nickel phosphide microstructures.[61] Thus, besides being a highly active OER electrocatalyst, the corner-etched PBAs-P is also revealed to exhibit a promising electrocatalytic performance toward HER. Encouraged by the promising bifunctional OER and HER performances of the corner-etched PBAs-P in alkaline media, we assembled an electrolytic cell by integrating two corner-etched PBAs-P electrodes as both the anode and cathode. Impressively, current densities of 10 and 20 mA cm^{-2} are attained at considerably low cell voltages of 1.64 and 1.73 V, respectively (Figure 5I). On the other hand, for a similar current density of 10 mA cm^{-2}, cross-PBAs-P and PBAs-P required cell voltages of 1.72 and 1.75 V, respectively. Subsequently, chromoamperometric test was also conducted on the electrolytic cell setup with corner-etched PBAs-P electrodes at constant potentials of 1.64 V over 45 h (Figure 5J). The cell showed long term sustained performances with no depreciation in current densities. This indicates the impressive long-term durability of the electrocatalyst for overall water splitting, and unveils corner-etched PBAs-P to be not only highly active, but also a very stable bifunctional electrocatalyst in alkaline media.

3 | CONCLUSION

In summary, iron phosphide with highly active, exposed $\{1\bar{2}0\}$ facets is preferentially prepared, making use of the labile coordination network of PBAs. The obtained corner-etched PBAs-P exhibits outstanding activity toward OER with a small Tafel slope of 45 mV dec^{-1} and an overpotential of 260 mV at a current density of 10 mA cm^{-2}, as well as remarkable electrochemical stability after long operation. Such impressive OER performance originating from the active sites can be attributed to its optimal reaction intermediates adsorption energy. Furthermore, the catalyst also demonstrates activity toward overall water splitting, requiring a small cell voltage of 1.64 V to drive a current density of 10 mA cm^{-2}. This work paves a new avenue towards the rational design and exploitation of metal organic frameworks for selective synthesis of highly active phosphide OER electrocatalysts.

ACKNOWLEDGMENTS

We acknowledge support from the Ministry of Education (MOE) Singapore, under AcRF Tier 2 (MOE2019-T2-1-179), NUS R&G Postdoc Fellowship Programme, A-0000065-44-00 and A*STAR under its 2019 AME IRG & YIRG Grant Calls, A2083c0059.

CONFLICT OF INTEREST

The authors declare no conflicts of interest.

ORCID

Ghim Wei Ho https://orcid.org/0000-0003-1276-0165

REFERENCES

1. Roger I, Shipman MA, Symes MD. Earth-abundant catalysts for electrochemical and photoelectrochemical water splitting. *Nat Rev Chem*. 2017;1(1):3-15. doi:10.1038/s41570-016-0003
2. Dresselhaus M, Thomas I. Alternative energy technologies. *Nature*. 2001;414(6861):332-337. doi:10.1038/35104599
3. An L, Hu Y, Li J, et al. Tailoring Oxygen Reduction Reaction Pathway on Spinel Oxides via Surficial Geometrical-Site Occupation Modification Driven by the Oxygen Evolution Reaction. *Adv Mater*. 2022;34(28):2202874. doi:10.1002/adma.202202874
4. Turner J, Sverdrup G, Mann MK, et al. Renewable hydrogen production. *Int J Energy Res*. 2008;32(5):379-407. doi:10.1002/er.1372
5. You B, Sun Y. Innovative Strategies for Electrocatalytic Water Splitting. *Acc Chem Res*. 2018;51(7):1571-1580. doi:10.1021/acs.accounts.8b00002
6. Jiao Y, Zheng Y, Jaroniec M, Qiao SZ. Design of electrocatalysts for oxygen-and hydrogen-involving energy conversion reactions. *Chem Soc Rev*. 2015;44(8):2060-2086. doi:10.1039/C4CS00470A
7. An L, Wei C, Lu M, et al. Recent Development of Oxygen Evolution Electrocatalysts in Acidic Environment. *Adv Mater*. 2021;33(20):2006328. doi:10.1002/adma.202006328
8. An L, Feng J, Zhang Y, et al. Epitaxial Heterogeneous Interfaces on N-$NiMoO_4$/NiS_2 Nanowires/Nanosheets to Boost Hydrogen and Oxygen Production for Overall Water Splitting. *Adv Funct Mater*. 2019;29(1):1805298. doi:10.1002/adfm.201805298
9. McCrory CCL, Jung S, Ferrer IM, Chatman SM, Peters JC, Jaramillo TF. Benchmarking hydrogen evolving reaction and oxygen evolving reaction electrocatalysts for solar water

splitting devices. *J Am Chem Soc*. 2015;137(13):4347-4357. doi:10.1021/ja510442p

10. Lee Y, Suntivich J, May KJ, Perry EE, Shao-Horn Y. Synthesis and activities of rutile IrO_2 and RuO_2 nanoparticles for oxygen evolution in acid and alkaline solutions. *J Phys Chem Lett*. 2012;3(3):399-404. doi:10.1021/jz2016507
11. Yilmaz G, Yam KM, Zhang C, Fan HJ, Ho GW. In situ transformation of MOFs into layered double hydroxide embedded metal sulfides for improved electrocatalytic and supercapacitive performance. *Adv Mater*. 2017;29(26):1606814-1606821. doi:10.1002/adma.201606814
12. Wang H, Lee HW, Deng Y, et al. Bifunctional non-noble metal oxide nanoparticle electrocatalysts through lithium-induced conversion for overall water splitting. *Nat Commun*. 2015;6(1):7261-7268. doi:10.1038/ncomms8261
13. Gao M-R, Liang JX, Zheng YR, et al. An efficient molybdenum disulfide/cobalt diselenide hybrid catalyst for electrochemical hydrogen generation. *Nat Commun*. 2015;6(1):5982-5988. doi:10.1038/ncomms6982
14. Kibsgaard J, Jaramillo TF. Molybdenum phosphosulfide: an active, acid-stable, earth-abundant catalyst for the hydrogen evolution reaction. *Angew Chem Int Ed*. 2014;53(52):14433-14437. doi:10.1002/anie.201408222
15. Lu M, An L, Yin J, et al. Electronic engineering of amorphous Fe–Co–S sites in hetero-nanoframes for oxygen evolution and flexible Al–air batteries. *J Mater Chem A*. 2022;10(37):19757-19768. doi:10.1039/D2TA00191H
16. Xu K, Ding H, Zhang M, et al. Regulating water-reduction kinetics in cobalt phosphide for enhancing HER catalytic activity in alkaline solution. *Adv Mater*. 2017;29(28):1606980-1606985. doi:10.1002/adma.201606980
17. Chung DY, Jun SW, Yoon G, et al. Large-scale synthesis of carbon-shell-coated FeP nanoparticles for robust hydrogen evolution reaction electrocatalyst. *J Am Chem Soc*. 2017;139(19):6669-6674. doi:10.1021/jacs.7b01530
18. Xia C, Jiang Q, Zhao C, Hedhili MN, Alshareef HN. Selenide-Based Electrocatalysts and Scaffolds for Water Oxidation Applications. *Adv Mater*. 2016;28(1):77-85. doi:10.1002/adma.201503906
19. Deng D, Novoselov K, Fu Q, Zheng N, Tian Z, Bao X. Catalysis with two-dimensional materials and their heterostructures. *Nat Nanotech*. 2016;11(3):218-230. doi:10.1038/nnano.2015.340
20. Cao B, Veith GM, Neuefeind JC, Adzic RR, Khalifah PG. Mixed close-packed cobalt molybdenum nitrides as non-noble metal electrocatalysts for the hydrogen evolution reaction. *J Am Chem Soc*. 2013;135(51):19186-19192. doi:10.1021/ja4081056
21. Wu HB, Xia BY, Yu L, Yu X-Y, Lou XWD. Porous molybdenum carbide nano-octahedrons synthesized via confined carburization in metal-organic frameworks for efficient hydrogen production. *Nat Commun*. 2015;6(1):6512-6519. doi:10.1038/ncomms7512
22. Vrubel H, Hu X. Molybdenum Boride and Carbide Catalyze Hydrogen Evolution in both Acidic and Basic Solutions. *Angew Chem Int Ed*. 2012;51(51):12703-12706. doi:10.1002/anie.201207111
23. Liu P, Rodriguez JA. Catalysts for hydrogen evolution from the [NiFe] hydrogenase to the Ni_2P (001) surface: the importance of ensemble effect. *J Am Chem Soc*. 2005;127(42):14871-14878. doi:10.1021/ja0540019
24. Popczun EJ, McKone JR, Read CG, et al. Nanostructured nickel phosphide as an electrocatalyst for the hydrogen evolution reaction. *J Am Chem Soc*. 2013;135(25):9267-9270. doi:10.1021/ja403440e
25. Ling T, Yan DY, Jiao Y, et al. Engineering surface atomic structure of single-crystal cobalt (II) oxide nanorods for superior electrocatalysis. *Nat Commun*. 2016;7(1):12876-12883. doi:10.1038/ncomms12876
26. Tian N, Zhou Z-Y, Sun S-G, Ding Y, Wang ZL. Synthesis of tetrahexahedral platinum nanocrystals with high-index facets and high electro-oxidation activity. *Science*. 2007;316(5825):732-735. doi:10.1126/science.1140484
27. Hu M, Furukawa S, Ohtani R, et al. Synthesis of Prussian Blue Nanoparticles with a Hollow Interior by Controlled Chemical Etching. *Angew Chem Int Ed*. 2012;51(4):984-988. doi:10.1002/anie.201105190
28. Hu M, Belik AA, Imura M, Yamauchi Y. Tailored design of multiple nanoarchitectures in metal-cyanide hybrid coordination polymers. *J Am Chem Soc*. 2012;135(1):384-391. doi:10.1021/ja3096703
29. Yilmaz G, Tan CF, Hong M, Ho GW. Functional defective metal-organic coordinated network of mesostructured nanoframes for enhanced electrocatalysis. *Adv Funct Mater*. 2018;28(2):1704177-1704185. doi:10.1002/adfm.201704177
30. Han L, Yu XY, Lou XWD. Formation of Prussian-blue-analog nanocages via a direct etching method and their conversion into Ni-Co-mixed oxide for enhanced oxygen evolution. *Adv Mater*. 2016;28(23):4601-4605. doi:10.1002/adma.201506315
31. Ren W, Qin M, Zhu Z, et al. Activation of sodium storage sites in prussian blue analogues via surface etching. *Nano Lett*. 2017;17(8):4713-4718. doi:10.1021/acs.nanolett.7b01366
32. Hu M, Ishihara S, Ariga K, Imura M, Yamauchi Y. Kinetically controlled crystallization for synthesis of monodispersed coordination polymer nanocubes and their self-assembly to periodic arrangements. *Chem A Eur J*. 2013;19(6):1882-1885. doi:10.1002/chem.201203138
33. Tian ZR, Voigt JA, Liu J, et al. Complex and oriented ZnO nanostructures. *Nat Mater*. 2003;2(12):821-826. doi:10.1038/nmat1014
34. Dong X, Ji X, Wu H, Zhao L, Li J, Yang W. Shape control of silver nanoparticles by stepwise citrate reduction. *J Phys Chem C*. 2009;113(16):6573-6576. doi:10.1021/jp900775b
35. Morris RE, Brammer L. Coordination change, lability and hemilability in metal–organic frameworks. *Chem Soc Rev*. 2017;46(17):5444-5462. doi:10.1039/C7CS00187H
36. Jones LH. Nature of bonding in metal cyanide complexes as related to intensity and frequency of infrared absorption spectra. *Inorg Chem*. 1963;2(4):777-780. doi:10.1021/ic50008a027
37. Jones LH, Swanson BI. Interpretation of potential constants: application to study of bonding forces in metal cyanide complexes and metal carbonyls. *Acc Chem Res*. 1976;9(4):128-134. doi:10.1021/ar50100a002
38. Goberna-Ferrón S, Hernández WY, Rodríguez-García B, Galán-Mascarós JR. Light-driven water oxidation with metal hexacyanometallate heterogeneous catalysts. *ACS Catal*. 2014;4(6):1637-1641. doi:10.1021/cs500298e
39. Wilde RE, Ghosh SN, Marshall BJ. Prussian blues. *Inorg Chem*. 1970;9(11):2512-2516. doi:10.1021/ic50093a027

40. Pasta M, Wessells CD, Liu N, et al. Full open-framework batteries for stationary energy storage. *Nat Commun*. 2014;5(1):3007-3015. doi:10.1038/ncomms4007
41. Dostal A, Kauschka G, Reddy SJ, Scholz F. Lattice contractions and expansions accompanying the electrochemical conversions of Prussian blue and the reversible and irreversible insertion of rubidium and thallium ions. *J Electroanal Chem*. 1996;406(1-2):155-163. doi:10.1016/0022-0728(95)04427-2
42. Cai D, Liu B, Wang D, et al. Rational synthesis of metal–organic framework composites, hollow structures and their derived porous mixed metal oxide hollow structures. *J Mater Chem A*. 2016;4(1):183-192. doi:10.1039/C5TA07085F
43. Zhang W, Zhao Y, Malgras V, et al. Synthesis of Monocrystalline Nanoframes of Prussian Blue Analogues by Controlled Preferential Etching. *Angew Chem Int Ed*. 2016;55(29):8228-8234. doi:10.1002/anie.201600661
44. Ye H, Chen J, Hu Y, et al. One-pot synthesis of two-dimensional multilayered graphitic carbon nanosheets by low-temperature hydrothermal carbonization using the in situ formed copper as a template and catalyst. *Chem Commun*. 2020;56(78):11645-11648. doi:10.1039/D0CC03010D
45. Zheng X, Lv W, Tao Y, et al. Oriented and Interlinked Porous Carbon Nanosheets with an Extraordinary Capacitive Performance. *Chem Mater*. 2014;26(23):6896-6903. doi:10.1021/cm503845q
46. Wang Y, Zhang L, Li H, et al. Solid state synthesis of Fe_2P nanoparticles as high-performance anode materials for nickel-based rechargeable batteries. *J Power Sources*. 2014;253:360-365. doi:10.1016/j.jpowsour.2013.12.056
47. Wang H, Xie Y, Cao H, et al. Flower-like nickel phosphide microballs assembled by nanoplates with exposed high-energy (001) facets: efficient electrocatalyst for the hydrogen evolution reaction. *ChemSusChem*. 2017;10(24):4899-4908. doi:10.1002/cssc.201701647
48. Griffith W. Cyanide complexes of the transition metals. *Quarterly Reviews Chem Soc*. 1962;16(2):188-207. doi:10.1039/qr9621600188
49. Huang Z, Lv C, Chen Z, Chen Z, Tian F, Zhang C. One-pot synthesis of diiron phosphide/nitrogen-doped graphene nanocomposite for effective hydrogen generation. *Nano Energy*. 2015;12:666-674. doi:10.1016/j.nanoen.2015.01.027
50. Qian M, Cui S, Jiang D, Zhang L, Du P. Highly efficient and stable water-oxidation electrocatalysis with a very low overpotential using FeNiP substitutional-solid-solution nanoplate arrays. *Adv Mater*. 2017;29(46):1704075-1704080. doi:10.1002/adma.201704075
51. Lu Y, Tu JP, Xiong QQ, et al. Controllable synthesis of a monophase nickel phosphide/carbon (Ni_5P_4/C) composite electrode via wet-chemistry and a solid-state reaction for the anode in lithium secondary batteries. *Adv Funct Mater*. 2012;22(18):3927-3935. doi:10.1002/adfm.201102660
52. Liu M, Yang L, Liu T, et al. Fe_2P/reduced graphene oxide/Fe_2P sandwich-structured nanowall arrays: a high-performance non-noble-metal electrocatalyst for hydrogen evolution. *J Mater Chem A*. 2017;5(18):8608-8615. doi:10.1039/C7TA01791J
53. Peng L, Shah SSA, Wei Z. Recent developments in metal phosphide and sulfide electrocatalysts for oxygen evolution reaction. *Chinese J Catal*. 2018;39(10):1575-1593. doi:10.1016/S1872-2067(18)63130-4
54. Liu K, Zhang C, Sun Y, et al. High-Performance Transition Metal Phosphide Alloy Catalyst for Oxygen Evolution Reaction. *ACS Nano*. 2018;12(1):158-167. doi:10.1021/acsnano.7b04646
55. Li G, Yang Q, Rao J, et al. In Situ Induction of Strain in Iron Phosphide (FeP_2) Catalyst for Enhanced Hydroxide Adsorption and Water Oxidation. *Adv Funct Mater*. 2020;30(12):1907791. doi:10.1002/adfm.201907791
56. Xiao P, Sk MA, Thia L, et al. Molybdenum phosphide as an efficient electrocatalyst for the hydrogen evolution reaction. *Energ Environ Sci*. 2014;7(8):2624-2629. doi:10.1039/C4EE00957F
57. Tian L, Yan X, Chen X. Electrochemical activity of iron phosphide nanoparticles in hydrogen evolution reaction. *ACS Catal*. 2016;6(8):5441-5448. doi:10.1021/acscatal.6b01515
58. Ledendecker M, Krick Calderón S, Papp C, Steinrück H-P, Antonietti M, Shalom M. The Synthesis of Nanostructured Ni_5P_4 Films and their Use as a Non-Noble Bifunctional Electrocatalyst for Full Water Splitting. *Angew Chem Int Ed*. 2015;54(42):12361-12365. doi:10.1002/anie.201502438
59. Li F, Bu Y, Lv Z, et al. Porous cobalt phosphide polyhedrons with iron doping as an efficient bifunctional electrocatalyst. *Small*. 2017;13(40):1701167-1701172. doi:10.1002/smll.201701167
60. Huang H, Yu C, Yang J, et al. Ultrasmall diiron phosphide nanodots anchored on graphene sheets with enhanced electrocatalytic activity for hydrogen production via high-efficiency water splitting. *J Mater Chem A*. 2016;4(41):16028-16035. doi:10.1039/C6TA05086G
61. Huang H, Yu C, Zhao C, et al. Iron-tuned super nickel phosphide microstructures with high activity for electrochemical overall water splitting. *Nano Energy*. 2017;34:472-480. doi:10.1016/j.nanoen.2017.03.016

SUPPORTING INFORMATION

Additional supporting information can be found online in the Supporting Information section at the end of this article.

How to cite this article: Yilmaz G, Yang T, Lim KJH, et al. Rational engineering of metal–organic coordination networks into facet-controlled phosphides for overall water splitting. *EcoMat*. 2023;5(3):e12312. doi:10.1002/eom2.12312